

Preparation and Properties of MOF-derived Porous Carbon Nanosheets as Electrocatalyst for Oxygen Reduction Reaction

Jing Zhang^{1,3}, Xiangzhi Meng², Qiuping Zhao^{2,*}

¹ National Nickel and Cobalt Advanced Materials Engineering Research Center

² School of Petrochemical Technology, Lanzhou University of Technology, Lanzhou 730050, China

³ Lanzhou Jinchuan Technology Park Co., Ltd., Gansu 730101, China

*E-mail: zqp_lz@163.com

Received: 16 May 2022 / Accepted: 16 June 2022 / Published: 7 August 2022

MOFs-derived nitrogen-doped porous carbon nanosheets Fe@Co/N@PCN were prepared by pyrolysis using Fe@Co/Zn-MOFs and g-C₃N₄ as precursor templates. The effects of metal doping on the catalytic activity of MOFs carriers were investigated by morphological structure and electrochemical performance characterization. It was found that the addition of bimetals not only increased the specific surface area of the catalysts, but also had a synergistic catalytic effect, resulting in a half-slope potential of 0.872 V vs. RHE in Fe@Co/N@PCN in 0.1 M KOH, and its ORR electrocatalytic activity, stability and methanol resistance were better than those of commercial Pt/C catalysts.

Keywords: Metal organic framework material, porous carbon nanosheets, double-metal, ORR

1. INTRODUCTION

Fuel cells rely significantly on electrocatalysts to accomplish the oxygen reduction reaction (ORR), which is driven by a succession of precious metal platinum-based catalysts. Noble metal ORR catalysts are now well researched due to their high catalytic activity, but Pt is expensive and readily poisoned during ORR, preventing fuel cell commercialisation[1,2].

Because of their enormous reserves, low price, strong catalytic activity, and consistent performance, non-precious metal catalysts have gotten a lot of attention in recent years. At present, non-noble metal ORR electrocatalysts with activity mainly include transition metal nanoparticles[3], Transition metal oxides[4], Nitride[5], Phosphide[6] and Carbide[7], etc. To boost electrocatalytic activity even more, the researchers created bimetallic catalysts that assist regulate the complex electrical structure and vary the surface chemistry, exposing additional active sites and increasing catalytic activity. Wang et al. showed that combining various transition metals in ORR electrocatalysts

has a synergistic impact that improves select-rocatalytic activity and electron transfer rate[8].However, carbon material catalysts prepared by transition metal nitrogen doping are prone to metal particle aggregation [9], large loss of dopant atoms[10], and low graphitization[11] after calcination, and in order to solve the above problems, it is necessary to select a suitable precursor metal organic frame (MOFs). MOFs are good precursors due to their well-defined pore structure and excellent conductivity of the carbonized products[12]. However, MOFs-derived carbon catalysts suffer from significant nitrogen loss during pyrolysis, which limits the formation of active sites. In this paper, a large number of nitrogen sources were added in the pyrolysis process of MOFS-derived carbon catalyst to prepare MOFS derived carbon materials with two-dimensional sheet structure. Two dimensional porous carbon nanosheets have the advantage of exposing more active centers to the reactants and lower diffusion resistance, which improves the utilization of catalytic sites and power density[13]. The bimetallic catalysts were prepared by a two-step hydrothermal method using Zn/Fe@Co-MOFs as precursors and g-C₃N₄ as nitrogen source, and the bimetallic catalysts were obtained after pyrolysis. The catalysts exhibited excellent ORR catalytic activity, durability and methanol resistance in 0.1 M KOH electrolyte.

2. EXPERIMENTAL SECTION

2.1 Preparation of Fe@Co/Zn-MOFs

60 mg of 1,4,5,8-naphthalenetetracarboxylic acid (NTCDA) was added to a solution containing 100 mL for 8 h until the solution became clear. Afterwards, 7.5 g of Zn(NO₃)₂·6H₂O was dissolved using 100 mL of deionized water and 50 mg of FeSO₄·6H₂O and 50 mg of Co(NO₃)₂·6H₂O were added to this solution. then the round bottom flask was sealed and stirred at 60 °C for 24 h. To obtain Zn/Fe@Co/Zn-MOFs, the precursors were separated by centrifugation, washed three times with deionized water, and dried under vacuum for 24 hours at 80 °C.

2.2 Preparation of g-C₃N₄ precursors

6 g melamine and 0.1 g glucose were dissolved in 30 mL ultrapure water, stirred for 1 h, and dried under vacuum at 80 °C to obtain solid (A).

2.3 Preparation of Fe@Co/N@PCN

Zn/Fe@Co/Zn-MOFs and A were ground well at 3:1, heated at 30 °C to 550 °C at 5 °C·min⁻¹ and held for 3 hours; then heated to 900 °C at 5 °C·min⁻¹ and held for 3 hours, and then naturally reduced to room temperature to obtain the catalyst Fe@Co/N@PCN.

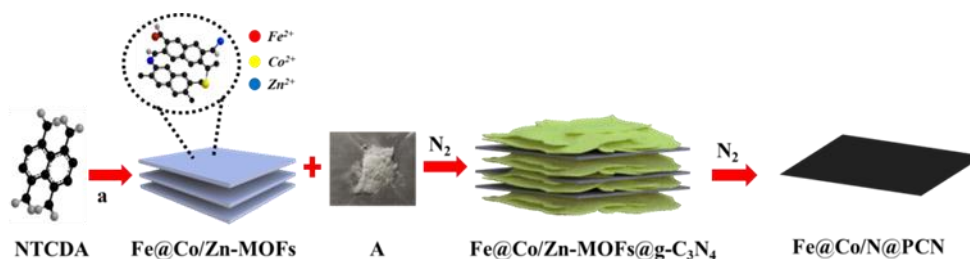


Figure 1. Synthesis schematic of Fe@Co/N@PCN

2.4 Preparation of working electrodes

(1) The functioning electrode is cleaned. It is necessary to clean the working electrode before proceeding. Use 0.05 μm polishing powder to polish the glassy carbon electrode on the buckskin cloth in the shape of "8" until the mirror surface is smooth, and then clean and wipe it in ethanol and water in turn, and dry it afterwards.

(2) The prepared sample catalyst was thoroughly ground. 5 mg catalyst was accurately weighed in a glass vial, 15.0 μL Nafion, 2.25 mL ethanol and 0.25 mL ultrapure water were measured with a pipette gun into the vial, and ultrasonic treatment was performed for 30 min to produce uniform ink.

(3) Coated electrode. The prepared ink was uniformly dripped onto the glassy carbon electrode. The sample catalyst was loaded with 1 mg cm^{-2} and commercial Pt/C was loaded with 0.1 mg cm^{-2} . The sample was irradiated to dry with an infrared lamp, and the ORR test was performed.

2.5 Electrochemical performance testing

2.5.1 Potential correction of the reference electrode

Potential calibration of the reference electrode is required before the electrochemical performance test, and the calibration procedure is as follows: using Pt electrode as the working electrode and Pt wire as the counter electrode, a linear scanning voltammetry (LSV) test is performed in hydrogen-saturated 0.1 M KOH or 0.1 M HClO₄ aqueous solution, and the thermodynamic potential of the H⁺/H₂ reaction when the scanning current is zero is recorded, and by virtue of this potential, the potential of the reference electrode and the reversible hydrogen electrode (RHE). Note: For the calomel electrode, the calibration is performed with the help of a salt bridge (consisting of agar and saturated potassium nitrate solution) with a 0.1 M HClO₄ aqueous solution forming a loop. See Table 1 for details.

Table 1. The calibration of Saturated calomel and Hg/HgO reference electrodes relative to RHE

Electrolytes	Reference electrode	thermodynamic potential	Correction formula
0.1 M KOH	Hg/HgO Electrodes	-0.889 V (vs.RHE)	$E(\text{RHE}) = E(\text{Hg}/\text{HgO}) + 0.889$
0.1 M HClO ₄	Glycerol electrode	-0.248 V (vs.RHE)	$E(\text{RHE}) = E(\text{calomel}) + 0.248$

2.5.2 Electrochemical test methods

In this experiment, cyclic voltammetry (CV), linear sweep voltammetry (LSV), methanol resistance and stability tests were performed on the prepared sample catalysts. The test procedures are as follows:

Cyclic voltammetry (CV): The Hg/HgO reference electrode and graphite rod counter electrode were inserted into an electrolytic cell with 0.1 M KOH electrolyte, and high purity nitrogen gas was passed below the liquid surface for 30 min until saturation, and the working electrode coated with catalyst was placed into the electrolytic cell, and CV activation was performed at a sweep speed of 100 mV for 10 turns. After the activation, a CV test was performed at a sweep rate of 50 mV for 10 turns as the background current.

Linear sweep voltammetry (LSV) testing: Same as CV venting, LSV data were measured for the working electrode as background current at different rotational speeds from 400, 900, 1600, 2025, 2500 rpm under saturated nitrogen atmosphere. subsequent operation under oxygen saturation was the same as for nitrogen. The voltage range was 0 ~ 1.2 V vs. RHE with a sweep speed of 5 mV/s. The tests in 0.1 M HClO₄ aqueous solution were identical to those in 0.1 M KOH aqueous solution.

Methanol resistance test: Ventilated as above, under saturated oxygen atmosphere, without turning on the rotational speed, tested by methanol cross-timed current method, adding 3 M of methanol solution to 0.1 M KOH electrolyte solution at 400 seconds, observing and recording the change of current density before and after the drop addition. The test in 0.1 M HClO₄ aqueous solution is the same as under 0.1 M KOH aqueous solution. Note: The anti-methanol test must be activated first.

Stability testing: After performing the complete CV and LSV, the catalyst was tested by the chrono-current method at a rotational speed of 1600 rpm and run under 0.1 M KOH aqueous solution for 10 hours to observe the loss of catalyst current density. The tests in 0.1 M HClO₄ aqueous solution were the same as those under 0.1 M KOH aqueous solution.

Commercial Pt/C catalysts (JM Pt/C 20 wt%) were used as the standard in this experiment, and all of the above tests were performed on the experimentally prepared catalysts alongside the commercial Pt/C catalysts, reflecting the oxygen reduction performance of the prepared catalysts by comparing the commercial Pt/C with the electrochemical test data of the prepared electrocatalysts. Currently, the evaluation criteria for evaluating the performance of oxygen reduction catalysts are limiting current density, half-wave potential, onset potential, number of transferred electrons and catalytic stability and methanol resistance. The performance of the sample catalysts can be visually assessed by comparing these test data of different catalysts.

3. RESULTS AND DISCUSSION

3.1 SEM and TEM analysis

In order to obtain the microscopic morphology and structure of Fe@Co/N@PCN, the precursors (Zn/Fe@Co/Zn-MOFs) of Fe@Co/N@PCN were observed by scanning electron microscopy. As shown in Figure 2a, the Zn/Fe@Co/Zn-MOFs exhibit a 2D nanosheet morphology with an average thickness

of 0.2 μm (Figure 2b). The derived catalyst Fe@Co/N@PCN kept its 2D nanosheet morphology well after pyrolysis (Figure 2c), but the surface of the catalyst became rougher and the thickness of the catalyst slightly decreased compared to the precursor, which was due to the decomposition of the MOFs material during the pyrolysis process, as shown in Figure 2d.

Table 2. Elemental content of Fe@Co/N@PCN

Element	Mass fraction/%	Atomic content/%
C	73.93	80.43
N	19.30	18.00
Fe	5.12	1.20
Co	1.65	0.37

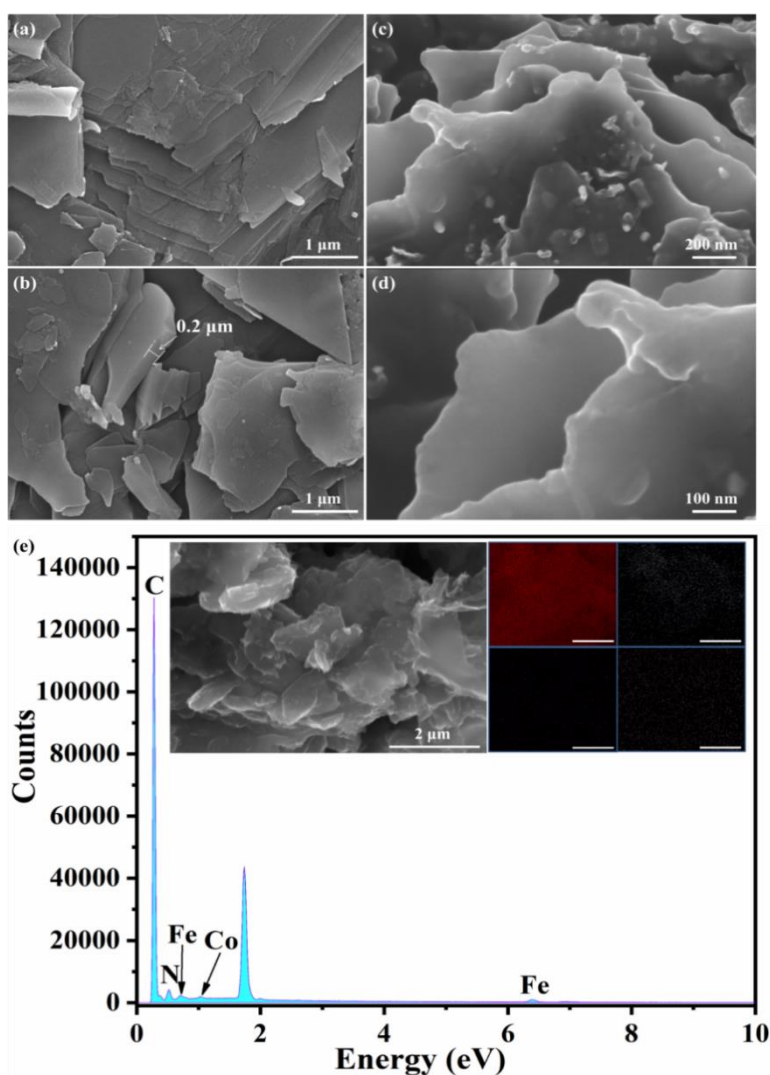


Figure 2. The SEM images of Zn/Fe@Co/Zn-MOFs (a, b); TEM images (c, d); EDX and EDS images (e) of Fe@Co/N@PCN

The mass contents of the elements in Fe@Co/N@PCN were 73.93 wt%, 19.30 wt%, 5.12 wt% and 1.65 wt%, respectively, as seen in the EDX and EDS test results (Figure 2e) (Table 1). The absence of the element Zn is due to the pyrolysis temperature reaching the boiling point of Zn, which evaporates away from the organic ligand during the pyrolysis process. Besides, the doped bimetals (Fe, Co) are highly dispersed in the catalyst (Figure 2e), which may be attributed to the fact that the zinc added during the preparation of MOFs acts as a segregation so that the Fe and Co atoms can be highly dispersed.

3.2 XRD and Raman analysis

To obtain the crystal structure of Fe@Co/N@PCN, the analysis was performed by XRD mapping. As shown in Figure 3a, g-C₃N₄ was not detected in Fe@Co/N@PCN (Figure 3b), which indicates that all precursors of g-C₃N₄ decompose to nitrogen-containing small molecule gases during high-temperature pyrolysis, providing a sufficient source of nitrogen for the catalyst to coordinate with Fe and Co atoms to form active sites (M-N_x, M = Fe, Co), and secondly Fe-N_x and Co-N_x have a synergistic effect to further enhance the catalytic activity of Fe@Co/N@PCN[14-16]. Furthermore, distinctive peaks of Fe₂O₃ (PDF#40-1139), Fe₃C (PDF#35-0772), and Co₃C (PDF#26-0450) showed in Fe@Co/N@PCN, showing the presence of other metal species in Fe@Co/N@PCN in addition to the active sites, which boosted the catalyst's conductivity. In order to clarify the degree of graphitization of the catalysts, Raman spectra were done for Fe@Co/N@PCN, Fe/N@PCN and Co/N@PCN, respectively. As shown in Figure 3c, Fe@Co/N@PCN has the smallest ratio of I_D/I_G and the highest degree of graphitization, which has a positive effect on the electron conductivity in the electrochemical reaction[17, 18].

3.3 BET and pore size distribution analysis

The nitrogen adsorption-desorption curves were used to determine the specific surface area and pore size distribution of Fe@Co/N@PCN, Fe/N@PCN, and Co/N@PCN. As shown in Figure 3d, all three catalysts exhibited a distinct type IV isotherm. The sharp increase in gas capacity at very low relative pressures ($P/P_0 < 0.05$) indicates the presence of a large number of micropores in the materials, while the presence of a significant H₄-type hysteresis line and fast adsorption at values of P/P_0 above 0.45 indicates the presence of mesoporous and macroporous structures in the materials, as shown in Table 3. The BET ratios of Fe@Co/N@PCN, Fe/N@PCN and Co/N@PCN surface areas of 417.7 m² g⁻¹, 64.4 m² g⁻¹ and 7.74 m² g⁻¹, respectively. The Fe@Co/N@PCN specific surface area increases noticeably, showing that both Fe and Co elements have a synergistic effect that efficiently improves the catalyst specific surface area. The adsorption pore volumes of Fe@Co/N@PCN, Fe/N@PCN and Co/N@PCN are 0.32 m³ g⁻¹, 0.07 m³ g⁻¹ and 0.06 m³ g⁻¹, respectively, calculated by BJH theory.

Figure 3e shows the pore size distribution of Fe@Co/N@PCN, Fe/N@PCN and Co/N@PCN. It can be seen that only Fe@Co/N@PCN has an absorption peak in the range of 2~20 nm, indicating that only a mesoporous structure exists within Fe@Co/N@PCN (Figure 3f). The pore structure can shorten the electron transport paths, allowing Fe/N@PCN to have excellent electrochemical properties. In view

of the above analysis, the larger specific surface area, abundant pore volume and high graphitization will increase the mass transport and conductivity. These properties lead to higher catalytic performance of Fe@Co/N@PCN in ORR.

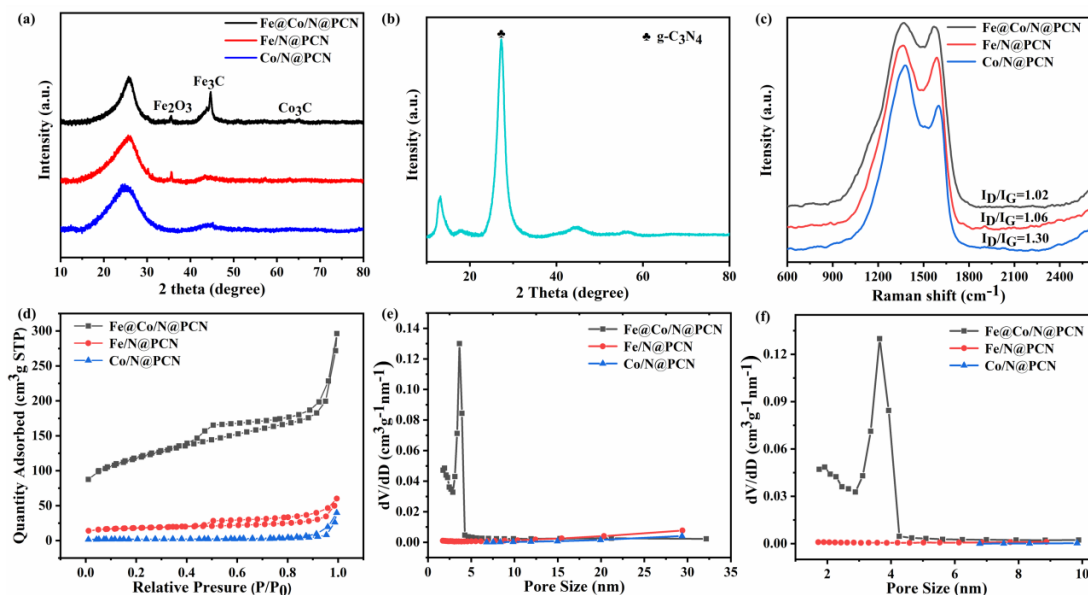


Figure 3. The XRD pattern: Fe@Co/N@PCN, Fe/N@PCN and Co/N@PCN(a); g-C₃N₄ (b); Raman pattern (c); N₂ adsorption-desorption isotherm (d); Pore size distribution (e, f) of Fe@Co/N@PCN, Fe/N@PCN and Co/N@PCN

Table 3. Surface areas and pore volumes of Fe@Co/N@PCN, Fe/N@PCN and Co/N@PCN

The Sample	BET/m ² g ⁻¹	Pore Volume/m ³ g ⁻¹
Fe@Co/N@PCN	417.7	0.32
Fe/N@PCN	64.4	0.07
Co/N@PCN	7.74	0.06

3.4 XPS analysis

In order to further analyze the composition and structure of Fe@Co/N@PCN, the samples were analyzed for elemental states using X-ray photoelectron spectroscopy (XPS), as shown in Figure 4. Figure 4a shows the full XPS spectrum of Fe@Co/N@GCN, and the results show the presence of five elements, C, O, N, Fe and Co, on its surface. It shows the presence of Fe and Co elements in Fe@Co/N@PCN, which is consistent with the test results of EDX and EDS. The high-resolution XPS spectrum of C 1s in Fe@Co/N@PCN (Figure 4b) shows three peaks: C-C/C=C (284.26 eV), C-OH/C-N (285.4 eV) and C-N (287.2 eV). In addition, the N 1s high-resolution XPS spectrum (Figure 4(c)) also shows peaks of four different N species at 398.3 eV, 399.1 eV, 399.6 eV, and 401.0 eV, which are peaks of pyridine-N, graphite-N, Fe-N, and Co-N, respectively[19-26]. According to a previously published

report, pyridine-N, Fe-N_x and Co-N_x are effective active sites in the ORR process[27]. On the other hand, graphite-N plays a key role in most nitrogen-doped carbon materials, where carbon atoms are linked to nitrogen atoms after the introduction of nitrogen molecules, showing higher positive charge density and stronger electron affinity in the overall material, thus improving the oxygen adsorption capacity and ORR catalytic performance.

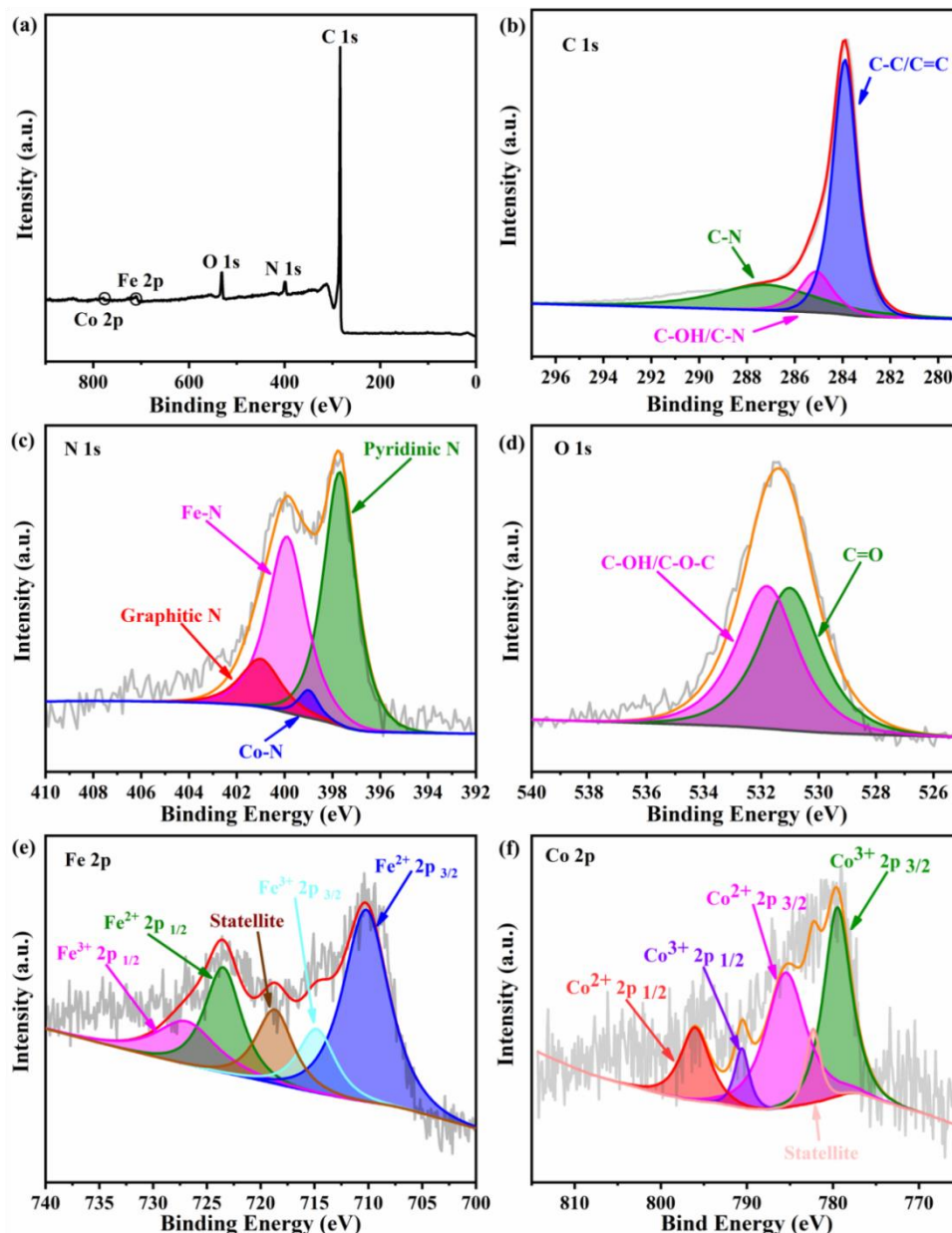


Figure 4. The Survey XPS spectra (a); High-resolution XPS spectra C 1s peaks (b); N 1s peaks (c); O 1s peaks (d); Fe 2p peaks (e); Co 2p peaks (f) of Fe/N@PCN

In addition, the high-resolution O 1s XPS spectrum (Figure 5.4d) reveals two types of O species: C=O (532.2 eV) and C-OH/C-O-C (533.0 eV), which implies the introduction of additional oxygen

species on the carbon surface, corresponding to the appearance of Fe_2O_3 in the XRD analysis map. The high-resolution XPS spectra of Fe 2p in Figure 5.4e appear as Fe $2p_{1/2}$ (Fe^{2+} : 724.2 eV and Fe^{3+} : 726.2 eV) and Fe $2p_{3/2}$ (Fe^{2+} : 710.8 eV and Fe^{3+} : 713.5 eV). The peak at 713.5 eV can also be considered as a characteristic peak corresponding to Fe- N_x species, which is the active center of the ORR process. Meanwhile, the XPS spectra of Co 2p in Figure 5.4f appear as Co $2p_{1/2}$ (Co^{2+} : 796.5 eV and Co^{3+} : 794.0 eV) and Co $2p_{3/2}$ (Co^{2+} : 784.5 eV and Co^{3+} : 780.0 eV). And the peak at 782.3 eV can also be considered as a characteristic peak corresponding to Co- N_x species, which is the active center of the ORR process.

3.5 Evaluation and analysis of electrochemical performance of catalysts

3.5.1 Evaluation of oxygen reduction catalytic activity

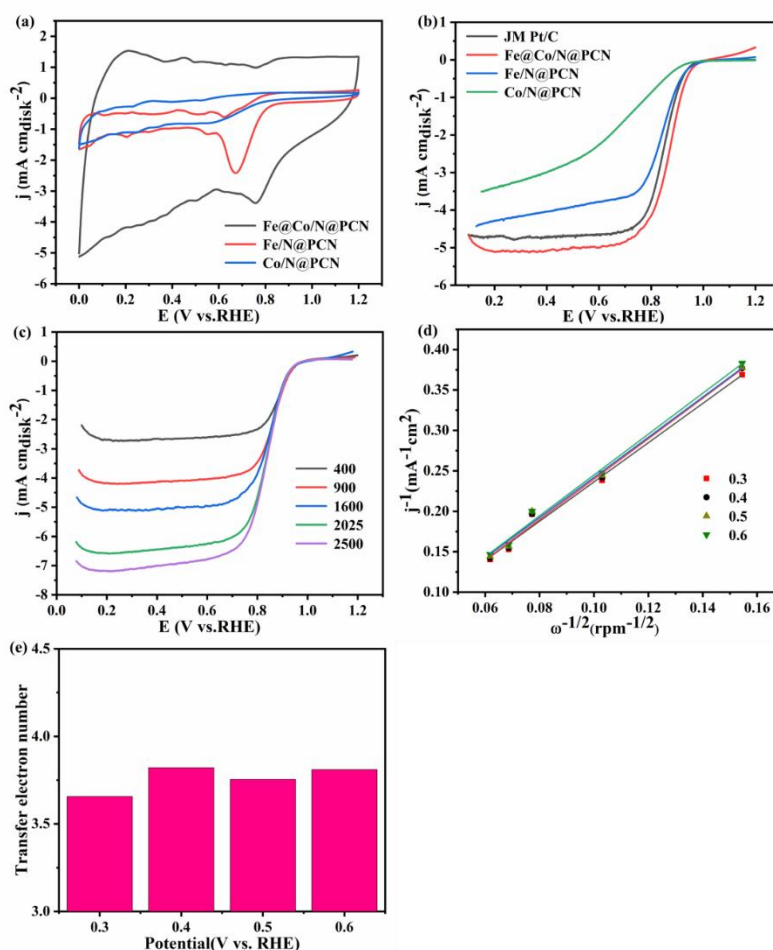


Figure 5. The CV curve (a) of Fe@Co/N@PCN, Fe/N@PCN and Co/N@PCN under N_2 and O_2 saturated 0.1 M KOH; LSV curve (b) of Fe@Co/N@PCN, Fe/N@PCN, Co/N@PCN and commercial Pt/C catalysts; LSV curve (c) of Fe@Co/N@PCN; K–L line (d); Electron transfer numbers (e)

The ORR performance was studied in 0.1 M KOH solution using a glassy carbon rotating disc electrode. First, the cyclic voltammetry (CV) curves were tested in an electrolyte saturated with O_2 and N_2 at 0.1 M KOH, and it can be seen from Figure 5a that obvious oxygen reduction peaks appear in the

CV curves of Fe@Co/N@PCN and Fe/N@PCN in the electrolyte at 0.1 M KOH, while no cathodic oxygen reduction peak appears for Co/N@PCN, which indicates that the catalysts Fe @Co/N@PCN and Fe/N@PCN have obvious oxygen reduction catalytic activity. However, it is noteworthy that the potential range of the cathodic oxygen reduction peak of Fe @Co/N@PCN is 0.586 ~ 0.880 V vs. RHE, while the potential range of the cathodic oxygen reduction peak of Fe/N@PCN is 0.58 ~ 0.80 V vs. RHE, which indicates that Fe@Co/N@PCN has higher oxygen reduction catalytic activity.

Table 4. ORR performance of Fe/N@GCN, Fe/N@PCN, Co/N@PCN and commercial Pt/C

The sample	The onset potential / V vs.RHE	Half-wave potential / V vs.RHE	Limiting current density / mA cm ⁻²
JM Pt/C	1.000	0.858	4.8
Fe@Co/N@PCN	1.018	0.872	5.1
Fe/N@PCN	0.978	0.846	4.4
Co/N@PCN	0.949	0.750	3.5

To further evaluate the ORR performance of the electrocatalyst, we performed linear sweep voltammetry (LSV) tests on the catalyst. As shown in Figure 5b, the onset potential, half-wave potential and limiting current density of Fe@Co/N@PCN in oxygen-saturated 0.1 M KOH electrolyte are higher than the values of Fe/N@PCN, Co/N@PCN and commercial Pt/C, The half-wave potential is 14 mV higher than that of commercial Pt/C, as shown in Table 4 LSV curves of Fe@Co/N@PCN were measured at different rotational speeds (400 ~ 2500 rpm) (Figure 5 c). It can be seen that the limiting current density of Fe@Co/N@PCN reaches 5.1 mA cm⁻² at 1600 RPM. In order to explore the electron transfer pathway of Fe@Co/N@PCN in ORR, the slope of Koutecky-Levich (Figure 5d) curve was extracted in the range of 0.3 ~ 0.7 V vs.RHE. The calculated electron transfer numbers (n) of Fe@Co/N@PCN at different voltages ranged from 3.66 ~ 3.82, indicating that the reaction process of Fe@Co/N@PCN catalyst was mainly 4e⁻ (Figure 5 e). All these results indicate that the pre-design of polymetallic precursors and the incorporation of g-C₃N₄ significantly improved the ORR electrocatalytic activity of the catalyst Fe@Co/N@PCN. The excellent electrocatalytic activity of Fe@Co/N@PCN can be attributed to several factors: (1) the synergistic effect of FeCo bimetallic atoms in the catalyst; (2) the large specific surface area, mesoporous structure and thickness of the 2D nanosheets (~20 μm), which not only promote mass diffusion but also increase the exposure of the active sites. The most important advantage of 2D catalysts over 3D catalysts is that the thickness is much thinner, which will allow easier diffusion of oxygen and electrolyte molecules and increase the reaction rate of ORR.

Table 5. ORR performance comparison between different catalysts and this work.

The sample	The onset potential / V vs.RHE	Half-wave potential / V vs.RHE	Reference
FeCo–NPC	0.97	0.87	[28]
CuCo@NC	0.96	0.884	[29]
CoOx/BNG	0.95	0.805	[30]
Co3O4–x/C	0.92	0.834	[31]
f C-MIL-101@PPy	0.959	0.828	[32]
Fe/Fe ₃ C@NC	0.85	0.7	[33]
Fe@Co/N@PCN	1.018	0.872	This work

3.5.2 Stability and methanol resistance test

In addition to good ORR catalytic activity, the stability of an excellent catalyst is also an important factor in the commercialization of a catalyst. The catalysts Fe@Co/N@PCN and commercial Pt/C were tested at 1600 RPM at a constant voltage of 0.8 V vs.RHE in a solution of 0.1 M KOH using timing current method (i-t). As shown in Figure 6a, Fe@Co/N@PCN has better stability, with only 11.5% drop in current density after 35,000 s, compared to 50.7% drop in current density for commercial Pt/C.

In addition, Fe@Co/N@PCN exhibited good methanol tolerance. As shown in Figure 6b, the current density of Fe@Co/N@PCN remained stable after a small transient fluctuation when 3 M methanol was rapidly injected into the 0.1 M KOH electrolyte at about 400 s. The current density remained at 94% of the initial value after 800 s. In contrast, the current density of commercial Pt/C electrolyte with the same concentration of methanol showed a significant On the contrary, the current density decayed significantly after adding the same concentration of methanol to the commercial Pt/C electrolyte, and the current density was only 48.4% of the initial value after 800 s. The above results indicate that Fe@Co/N@PCN has good ORR catalytic activity, stability and methanol resistance, and is a potentially suitable carbon-based ORR catalyst for methanol fuel cells.

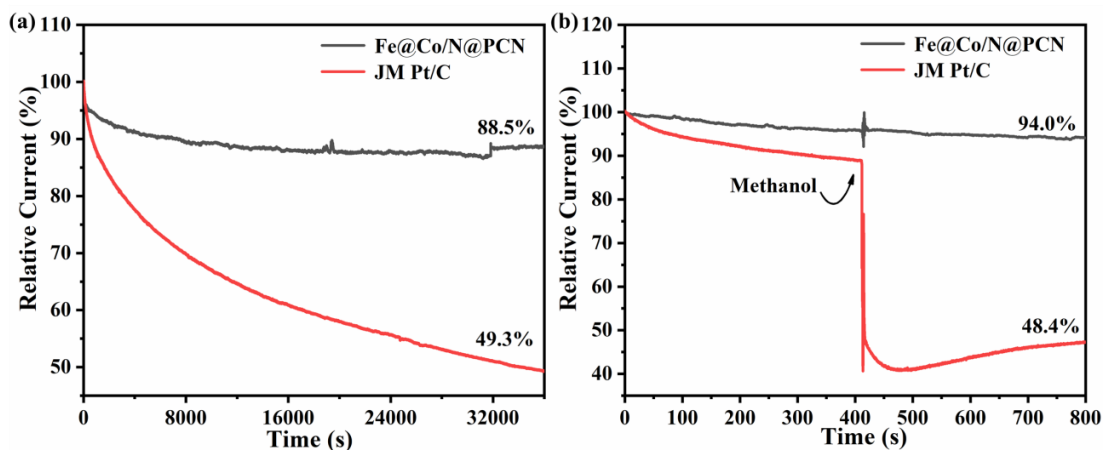


Figure 6. The *i*-*t* curves (a) of the Fe@Co/N@PCN and commercial Pt/C at 0.1 M KOH; the chronoamperometric response (b) of the Fe@Co/N@PCN and commercial Pt/C before and after the addition of 3 M methanol with a rotation speed of 1600 rpm at 0.80 V vs. RHE

4. CONCLUSION

In this chapter, a nitrogen-doped Fe, Co bimetallic porous carbon nanosheet catalyst containing Fe@Co/N@PCN was prepared. The precursor of g-C₃N₄ as a nitrogen source provides nitrogen-containing small molecules during catalyst pyrolysis that can anchor the active Fe and Co atoms to form the ORR catalytic active site M-N_x (M = Fe, Co), which is also confirmed by the characterization results of XRD and XPS. The analysis of Fe@Co/N@PCN by Raman and BET results showed better graphitization and larger specific surface area. This enabled it to show excellent ORR electrocatalytic performance in alkaline electrolytes with an onset potential of 1.018 V vs. RHE at 0.1 M KOH, 18 mV higher than that of commercial Pt/C; a half-wave potential of 0.872 V vs. RHE. Importantly, Fe@Co/N@PCN has excellent stability and methanol resistance.

ACKNOWLEDGEMENTS

This work was partially supported by 1. Lanzhou open competition mechanism, merit based admission project Major Fund; 2. the Natural Science Foundation of Gansu Province (20JR5RA441).

References

1. Y. T. Zhang, P. Wang, J. Yang, K. K. Li, X. Y. Long, M. Li, K. B. Zhang and J. S. Qiu, *Chemical Engineering Journal*, 401(2022) 126001.
2. G. Wu, K. L. More, C. M. Johnston and P. Science, 332(2011) 443.
3. X. X. Zheng, H. J. Niu, J. J. Feng, Q. L. Zhang, H. Huang, A. J. Wang, *Journal of Colloid and Interface ence*, 552(2019)744.
4. G. Janani, H. Choi, S. Surendran and U. Sim. , *MRS Bulletin*, 45(2020) 539.
5. M. D. Meganathan, S. Mao, T. Z. Huang and G. X. Sun. , *Journal of Materials Chemistry A*, 5(2017) 2972.
6. B. Nourmohammadi Khiarak, M. Golmohammad, M. M. Shahraki and A. Simchi, *Journal of*

Alloys and Compounds, 875(2021) 160049.

7. Y. Deng, B. Chi, J. Li, G. H. Wang, L. Zheng, X. D. Shi, Z. M. Cui, L. Du, S. J. Liao, K. Zang, J. Luo, Y. F. Hu and X. L. Sun, *Advanced Energy Materials*, 9(2019) 1802856.
8. Y. Wang, Y. Pan, L. K. Zhu, H. H. Yu, B. Y. Duan, R. W. Wang, Z. T. Zhang and S. L. Qiu, *Carbon*, 146(2019) 671.
9. K. Shen, L. Chen, J. L. Long, W. Zhong and Y. W. Li, *ACS Catalysis*, 5(2015) 5264.
10. P. Yin, T. Yao, Y. Wu, L. R. Zheng, Y. Lin, W. Liu, H. X. Ju, J. F. Zhu, X. Hong, Z. X. Deng, G. Zhou, S. Q. Wei and Y. D. Li, *Angewandte Chemie International Edition*, 2016, 55(2016) 10800.
11. R. Fang, R. Luque, Y. Li, *Green Chemistry*, 18(2016) 3152.
12. J. Gu, C. S. Hsu, L. Bai, H. M. Chen and X. L., *Science*, 364(2019) 1091.
13. K. Wan, A. D. Tan, Z. P. Yu, Z. X. Liang, J. H. Piao and P., *Applied Catalysis B Environmental*, 209(2017) 447.
14. G. Chen, P. Liu, Z. Liao, F. F. Sun, Y. H. He, H. X. Zhong, T. Zhang, E. Zschech, M. W. Chen, G. Wu, J. Zhang and X. L. Feng, *Advanced Materials*, 32(2020) 1907399.
15. R. Liu, D. Wu, X. Feng and K. Müllen, *Angewandte Chemie*, 49(2010) 2565.
16. Y. Hua, T. Jiang, K. Wang, M. M. Wu, S. Q. Song, Y. Wang, and P. Tsiakaras, *Applied Catalysis B Environmental*, 194(2016) 202.
17. A. D. Wang, Y. Fang, Z. Y. Liang, *CATALYSIS SCIENCE AND TECHNOLOGY*, 8(2018) 335.
18. L. L. Chai, Z. Y. Hu, X. Wang, L. J. Zhang, T. T. Li, Y. Hu, J. Q. Pan, J. J. Qian and S. M. Huang, *Carbon*, 174(2021) 531.
19. H. F. Wang, L. Chen, H. Pang, *Chemical Society Reviews*, 49(2020) 1414.
20. K. Aram, M. Nallal, Y. Chohye, *Nanomaterials*, 8(2018) 138.
21. M. Wu, K. Wang, M. Yi, Y. Tong, Y. Wang, *ACS Catalysis*, 7(2017) 6082.
22. H. Gao, Y. Ma, Y. Li, *Inorganic Chemistry Communications*, (2020) 108330.
23. S. Agarwal, X. Yu, A. Manthiram, *Materials Today Energy*, 16(2020) 100405.
24. M. Jahan, Q. Bao, K. P. Loh, *Journal of the American Chemical Society*, 134(2012) 6707.
25. Q. Ren, H. Wang, X. F. Lu, *Advanced ence*, (2018) 1700515.
26. K. Noaman, S. Saim, X. Shi, *Key Engineering Materials*, 778(2018) 275.
27. S. Lu, Z. Zhuang, *Journal of the American Chemical Society*, 139(2017) 5156.
28. X. Fang, L. Jiao, S.-H. Yu and H.-L. Jiang, *ChemSusChem*, 10 (2017) 3019.
29. M. Kuang, Q. Wang, P. Han and G. Zheng, *Adv. Energy Mater.*, 7 (2017) 1700193.
30. Y. Tong, P. Chen, T. Zhou, K. Xu, W. Chu, C. Wu and Y. Xie, *Angew. Chem. Int. Ed.*, 56 (2017) 7121.
31. D. Ji, L. Fan, L. Tao, Y. Sun, M. Li, G. Yang, T. Q. Tran, S. Ramakrishna and S. Guo, *Angew. Chem. Int. Ed.*, 58 (2019) 13840-13844.
32. T. Tan, P. Tao, X. Li, *Catalysis Communications*, 146(2020) 106135.
33. L. Yan, J. Zhang, K. Maryam, *Industrial & Engineering Chemistry Research*, 57(2018) 2744.

© 2022 The Authors. Published by ESG (www.electrochemsci.org). This article is an open access article distributed under the terms and conditions of the Creative Commons Attribution license (<http://creativecommons.org/licenses/by/4.0/>).